ACS NANO

www.acsnano.org

Sub-Band Filling, Mott-like Transitions, and Ion Size Effects in C_{60} Single Crystal Electric Double Layer Transistors

Tao He* and C. Daniel Frisbie*

Cite This: ACS Nano 2022, 16, 4823−4830

Read Online

ACCESS | Metrics & More | Article Recommendations | Supporting Information

ABSTRACT: **Electric double layer transistors (EDLTs) based on C_{60} single crystals and ionic liquid gates display pronounced peaks in sheet conductance versus gate-induced charge. Sheet conductance is maximized at electron densities near 0.5 e/C_{60} and is suppressed near 1 e/C_{60}. The conductance suppression depends markedly on the choice of ionic liquid cation, with small cations favoring activated transport and essentially a complete shutdown of conductance at ∼1 e/C_{60} and larger cations favoring band-like transport, higher overall conductances at all charge densities up to 1.7 e/C_{60}, and weaker suppression at 1 e/C_{60}. Displacement current measurements on C_{60} EDLTs with small cations show clear evidence of sub-band filling at 1 e/C_{60}, which correlates very well with the minimum in the C_{60} sheet conductance. Overall, the data suggest a significant Mott-Hubbard-like energy gap opens up in the surface density of states for C_{60} crystals gated with small cations. The causes of this energy gap may include both electron−electron repulsion and electron-cation attraction at the crystal/ionic liquid interface. The energy gap suppresses the insulator-to-metal transition in C_{60} EDLTs, but it can be manipulated by choice of electrolyte.**

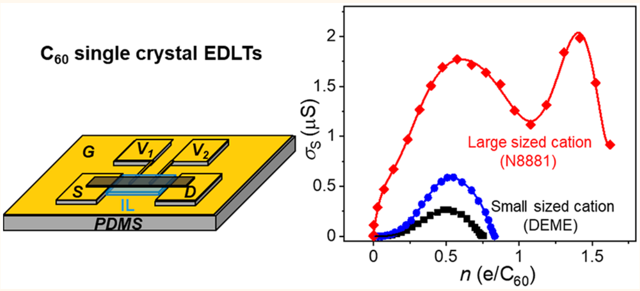

KEYWORDS: *C_{60} single crystal, electric double layer transistor, ionic liquid, ion size, electron−ion interaction, Mott transition, charge transport*

Electric double layer transistors (EDLTs) in which the gate insulator layer is a high-capacitance electrolyte are now commonly employed to explore two-dimensional (2D) transport physics and magnetism in a variety of materials at carrier densities >10^{14} cm^{-2}.[1−4] This carrier density is at least an order of magnitude greater than can be achieved in conventional field effect transistors (FETs) with SiO_2 gate dielectrics, for example. Researchers have demonstrated gate-induced insulator-to-metal transitions (IMTs), superconductivity, or ferromagnetism in EDLTs based on metal oxides,[5−11] metal sulfides,[12−18] and 2D materials such as graphene,[19,20] tellurene,[21,22] and MoS_2.[23] EDLTs have also been employed to examine charge ordering phenomena, Mott physics, and very recently an IMT in organic conductors.[24−28] Here we report EDLT measurements on single crystals of the well-known organic semiconductor C_{60}, Figure 1a. C_{60} is an intriguing choice for EDLT transport measurements as it is known to undergo a chemical doping-induced IMT and a metal-to-superconductor transition at 3 electrons/molecule.[29−32] Because C_{60} is a large molecule (radius r_{C60} = 0.35 nm), the molecular density of the (111) close-packed plane of face centered cubic (FCC) C_{60} crystals is relatively low at 1.1 × 10^{14} cm^{-2}, which is comparable to the achievable 2D charge densities in EDLTs. Thus, based on carrier considerations only, it seems that a gate-induced IMT might be achieved. It is noteworthy that EDLTs allow continuous control of 2D carrier density and thus in principle can access ranges of charge concentration that are difficult to achieve in chemical (e.g., alkali metal) doping studies of C_{60} due to phase separation.[32−34] Another distinguishing characteristic of EDLTs is that the 2D double-layer charging occurs without the intercalation and lattice expansion that are characteristic of chemical doping, and which are known to be important factors in the electronic phase behavior of doped C_{60}.[35,36]

It is also known from prior work that EDLTs based on organic materials often show a pronounced maximum in the sheet conductance versus charge relationship.[37−40] That is, beyond

Received: January 8, 2022
Accepted: February 24, 2022
Published: March 4, 2022

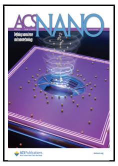

ACS Publications

https://doi.org/10.1021/acsnano.2c00222

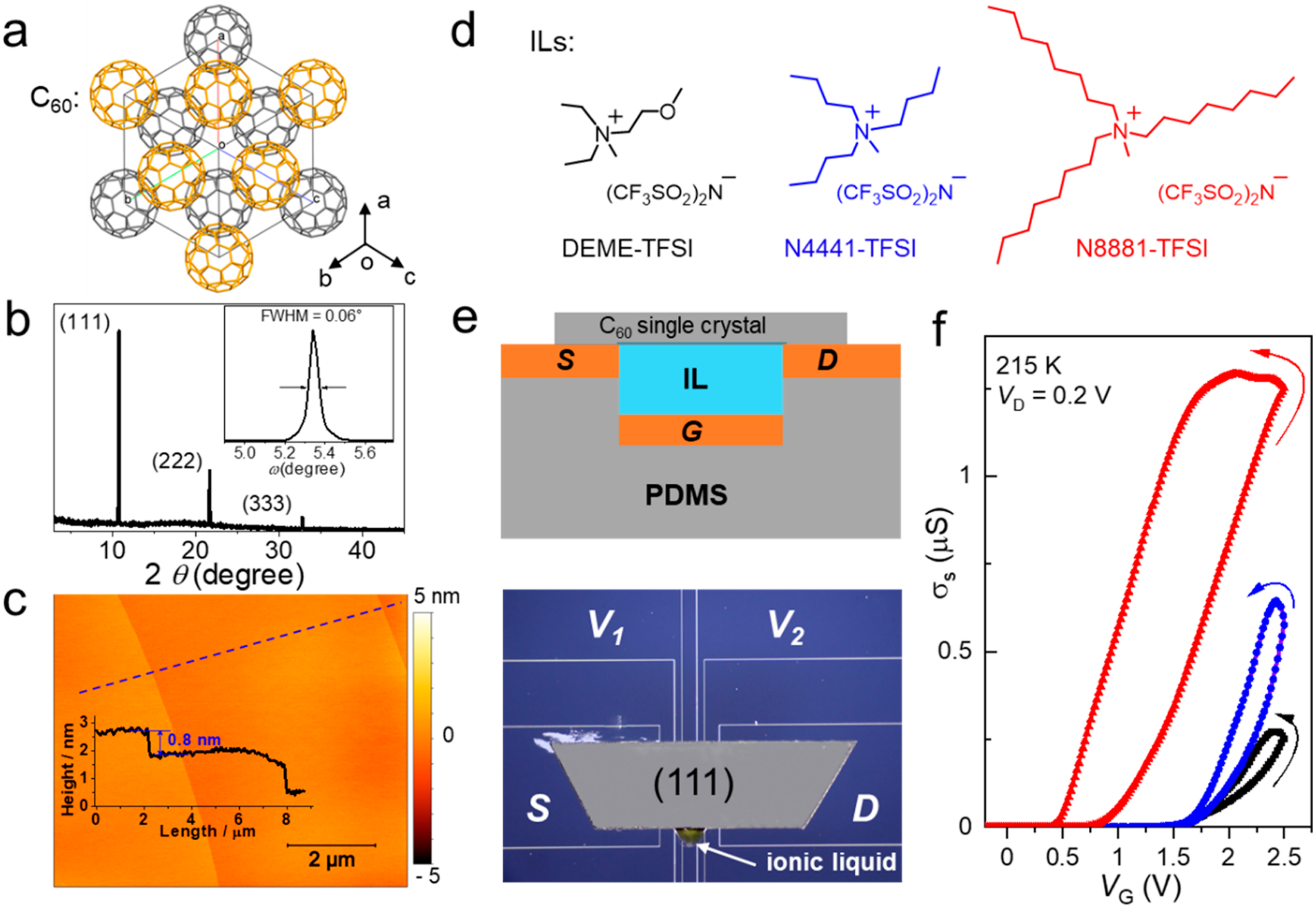

Figure 1. C_{60} **single crystal EDLTs. (a)** C_{60} **crystal structure viewed along [111]. Orange and gray colored molecules represent upper and lower molecular layers corresponding to adjacent (111) planes. (b) Out of plane XRD showing that the primary crystal facet corresponds to the (111) close packed plane. (inset) Rocking curve for the (111) peak. (c) AFM height image of the (111) facet. (inset) AFM height profile along the blue dashed line showing a single molecule tall step. (d) Molecular structures of three ionic liquids. (e) Cross-sectional schematic diagram of a** C_{60} **single crystal EDLT (top) and corresponding top-view optical micrograph (bottom). Channel electrodes** V_1 **and** V_2 **for four terminal measurements are evident in the micrograph. The gate-to-crystal gap is 5 μm. (f)** σ_s **as a function of** V_G **for** C_{60} **single crystal EDLTs gated by different ILs (DEME-TFSI, black; N4441-TFSI, blue; N8881-TFSI, red) at ∼215 K. The sweep rate is 20 mVs**$^{-1}$**.**

some critical carrier density, the conductance falls dramatically with further increases in gate-induced charge. This is well-exemplified by EDLTs based on rubrene crystals, where a peak in hole mobility versus gate voltage was confirmed by Hall effect measurements.[40,41] The collapse of mobility at high hole density suppresses the transition to a metallic state in rubrene. However, at the carrier density corresponding to peak mobility (0.15 holes per rubrene), a negative temperature coefficient of resistance is observed down to 120 K, and the resistance minimum is within a factor of 2 of h/e^2.[36] It seems that the IMT is narrowly missed in rubrene EDLTs.

We speculate that suppression of carrier mobility in organic EDLTs is related to ion-carrier interactions at the electrolyte/organic semiconductor interface;[40,42,43] the role of ion packing on transport in EDLT channels has been considered by others for inorganic materials.[15,44,45] Here, we explicitly examine the role of cation size on the n-channel conduction behavior of single crystal C_{60} EDLTs. We find that sheet conductance, electron mobility, and double layer capacitance are all functions of cation radius of the electrolyte. For the smallest cations, a clear peak in the sheet conductance curve is measured and conductance becomes fully suppressed at a charge density near one electron per C_{60}. However, increasing the cation size decreases the extent of suppression dramatically and allows us to explore transport up to 1.7 electrons/C_{60}. Technical challenges have kept us from making measurements down to low temperatures at these carrier densities, and those studies are ongoing. However, the cation size effect is important in its own right as it clearly has a striking impact on 2D electronic transport—and it is the focus of this report.

RESULTS AND DISCUSSION

Lath-like single crystals of C_{60} were grown by physical vapor transport (PVT) under an inert atmosphere and were characterized by X-ray diffraction and atomic force microscopy, Figure 1a−c (see also the Supporting Information, Figure S1 and S2).[46] The principal crystal faces corresponded to the close-packed (111) planes and were smooth with moderate molecular step densities (<2 steps/10 μm). Four terminal field effect transport (FET) measurements were made on the crystals using the vacuum gap FET platform with Au source and drain contacts. Typical four terminal field effect electron mobilities were gate voltage dependent and ranged as high as 2.5 cm^2 V^{-1} s^{-1} but were more typically ∼1 cm^2 V^{-1} s^{-1} (see Figure S3). Single crystal C_{60} EDLTs were made from the FETs using methods similar to those reported previously for rubrene

https://doi.org/10.1021/acsnano.2c00222
ACS Nano 2022, 16, 4823−4830

EDLTs.[38,41,42] Briefly, a drop of chilled ionic liquid was inserted into the gap between the C_{60} crystal and the recessed gate electrode, as shown in Figure 1e. Capillary forces aided insertion and drew the ionic liquid into the gap space. The ionic liquid transfer was accomplished in an inert atmosphere with the device held at 270 K on a probe station stage. After the liquid was inserted into the gap, the stage temperature was immediately dropped to ~215 K, just above the ionic liquid freezing point (Figure S4). Assembly and operation well below room temperature were necessary to obtain reproducible devices; we observed that room temperature operation of the EDLTs led to irreversible degradation (see Figure S5). This is different from rubrene EDLTs, which we found could be assembled and operated at room temperature without degradation over a defined gate voltage (V_G) window.[38,43]

Three different ionic liquids were utilized in the C_{60} EDLTs, DEME-TFSI [diethylmethyl(2-methoxyethyl)ammonium bis(trifluoromethylsulfonyl)imide], N4441-TFSI [tributylmethylammonium bis(trifluoromethylsulfonyl)imide], and N8881-TFSI [trioctylmethylammonium bis(trifluoromethylsulfonyl)imide]; their chemical structures are shown in Figure 1d. The TFSI anion was identical in each case. Each of these ionic liquid electrolytes is an ammonium salt where the positive charge lies on the core N atom and the alkyl chains provide a sterically bulky shell that separates the positive charge from neighboring ions or proximal interfaces.[47] One can estimate a cation radius from the liquid densities and computer simulations (ChemBio3D) and the maximum two-dimensional projected area A_{cation} can then be directly compared to the projected area of a single C_{60} molecule (A_{C60}), as shown in Table 1. Importantly, the circular area enclosing the N8881 cation is far larger than a C_{60} molecule, whereas the DEME and N4441 cations are smaller than C_{60} (see Figures S6 and S7 and Table 1).

Table 1. Comparison of C_{60} Single Crystal EDLT Parameters with Different ILs

	DEME	N4441	N8881
σ_s (μS)[a]	0.21 ± 0.07	0.55 ± 0.10	1.53 ± 0.10
n (10^{13} cm^{-2})[a]	5.2 ± 0.4	4.7 ± 0.3	4.1 ± 0.3
$n_{\max}$ (10^{13} cm^{-2})	8.1 ± 0.5	9.3 ± 0.4	18.8 ± 0.9
μ (cm^2 V^{-1} s^{-1})	0.03 ± 0.01	0.08 ± 0.03	0.21 ± 0.05
V_T (V)	1.75 ± 0.2	1.45 ± 0.25	1.10 ± 0.25
C_i (μF cm^{-2})[b]	7.8 ± 1.0	6.7 ± 1.2	5.8 ± 0.8
$A_{\text{cation}}/A_{C60}$	0.4	0.8	2.7

[a] σ_s and n were extracted at V_G = +2.5 V. [b] The capacitance was extracted in the linear region of the n−V_G plot using the equation $C_i = e(\partial n/\partial V_G)$.

Figure 1f shows typical four-terminal sheet conductance (σ_s) versus gate voltage (V_G) sweeps for C_{60} EDLTs based on the three different ionic liquids at 215 K. Counterclockwise hysteresis is observed in all sweeps due to the low temperatures and the corresponding sluggish ion transport which delays double layer formation and annihilation.[41] At 215 K the σ_s−V_G behavior is reproducible and it is always the case that at positive gate voltages σ_s is higher for the EDLTs with N8881-TFSI ionic liquid than for devices with the N4441-TFSI and DEME-TFSI ionic liquids. The fact that the transistors turn on for positive V_G values is consistent with electron accumulation, as expected. The low voltages required reflect the extremely large ionic liquid capacitances (≥5 μF cm^{-2}).

Figure 2 depicts a complete data set for C_{60} EDLTs employing the DEME-TFSI ionic liquid. In particular, Figure 2a displays the results for 50 continuous σ_s vs V_G sweeps (at 20 mV s^{-1}) out to V_G = +2.5 V at 215 K. The results indicate that the EDLTs are stable. Figure 2b shows the gate displacement current I_{disp} vs V_G for the same device at different sweep rates. These curves reveal the electron accumulation and depletion process as V_G is cycled from potentials negative of threshold out to +2.5 V and then back below threshold.[38] One clearly sees the onset voltage at which the channel opens and closes, in this case just positive of V_G = +1 V. As we have demonstrated previously for rubrene EDLTs, integration of I_{disp}−V_G traces (see shaded area) yields a reliable measure of total gate-induced charge in the semiconductor channel.[38] The total electron accumulation as a function of gate voltage is indicated by the blue trace in Figure 2b. It increases linearly with V_G, allowing a double-layer capacitance of 7.8 μF cm^{-2} to be extracted (Table 1). An electron density $n = 5.2 \times 10^{13}$ cm^{-2} is achieved at V_G = +2.5 V, which corresponds to nearly 0.5 e/C_{60} molecule (see also Figure S8).

Figure 2c displays the drain current I_D−V_G and σ_s−V_G behavior for excursions to larger gate voltages, V_G = +4 V. Over this larger V_G range, we observe striking behavior: there is a pronounced peak in I_D and σ_s that occurs at V_G = +2.65 V on the forward sweep. The peak is also evident in the reverse sweep but shifted negatively by ~0.7 V as shown. The collapse in I_D and σ_s at high gate voltages is more pronounced than in rubrene EDLTs;[40,41] 2D conductivity on C_{60} surfaces is essentially shut off. Note that on the semilog I_D−V_G plot in Figure 2c (black trace) one can see that the difference between the peak current and the current at V_G = +4 V is nearly a factor of 10^3.[15] Figure 2d displays the corresponding displacement current (I_{disp}) measurement over the same V_G range. We observe that I_{disp} is also strongly peaked. Integration of I_{disp} leads correspondingly to a plateauing of the n−V_G relationship (blue trace), which is unusual for EDLTs. Because the accumulated electron density reflects the 2D density of electronic states (DOS) on the crystal surface, the peak in the I_{disp}−V_G plot suggests that an electronic sub-band has been filled, or nearly so.[48,49] Integration of I_{disp} to V_G = +4 V yields a maximum $n = 8.5 \times 10^{13}$ cm^{-2} or ~0.8 e/C_{60} at the surface. Additionally, we observe that the peak in σ_s in Figure 2c aligns very well with the peak in I_{disp} (vertical dashed gray line) and corresponds to n = 0.5 e/C_{60}. The correspondence of the peak in σ_s with the peak in I_{disp} can be anticipated in a band-filling situation, as one would expect peak conductance near the maximum in the DOS. We return to this point later. To summarize the observations in Figure 2, we observed maximal conductance at 0.5 e/C_{60} and complete shut-off of conductance just under 1 e/C_{60}. We note that we have carefully examined contact resistance effects and sweep rate dependence of these results, and we definitively conclude that the current suppression is not tied to contact resistance or sweep rates (see Figures S9 and S10).

More insight is provided by similar data sets for C_{60} EDLTs with the N4441-TFSI and N8881-TFSI electrolytes, Figure 3. Figure 3a,b shows the log I_D−V_G and linear I_{disp}−V_G characteristics for EDLTs with N4441-TFSI. Again, a peak in I_D is observed, this time at V_G = +2.85 V on the forward sweep, again corresponding to ~0.5 e/C_{60}. The I_{disp}−V_G trace is also peaked, with the maximum in I_{disp} corresponding very nearly to the peak in I_D. Total induced charge plateaus again at n = 0.8e/C_{60} = 9×10^{13} cm^{-2}. In the linear portion of the n−V_G relationship, we estimate the double layer capacitance to be

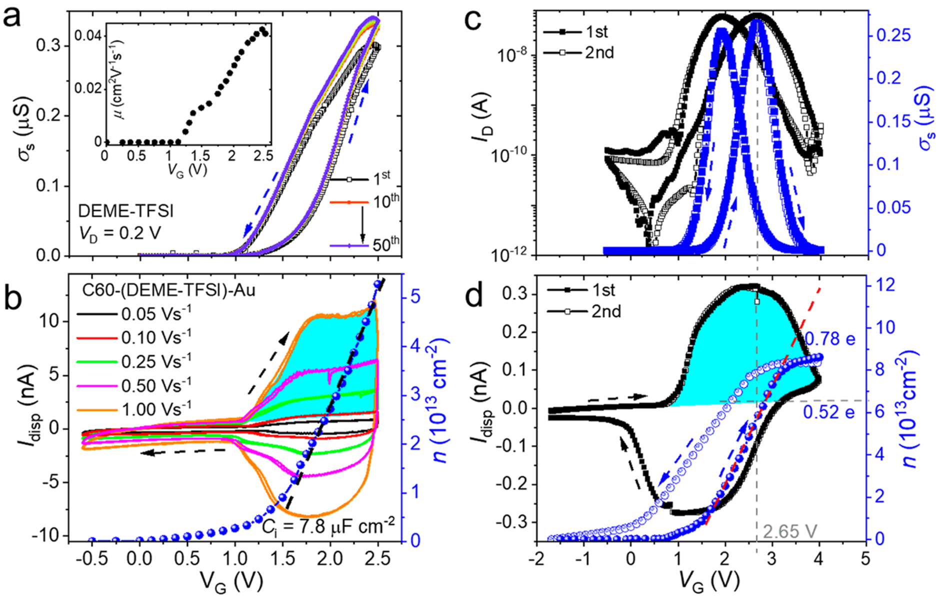

Figure 2. Electrical characterization of C_{60} single crystal EDLTs gated with DEME-TFSI at 215 K. (a) Sheet conductance σ_s vs V_G up to $V_G = 2.5$ V with $V_D = 0.2$ V. Hysteresis is counter clockwise. (inset) Estimated four terminal mobility as a function of V_G. (b) Corresponding $I_{disp}-V_G$ measurements at different V_G sweep rates. Also shown is the corresponding $n-V_G$ plot determined by integration of I_{disp} as shown in blue. (c) I_D-V_G and σ_s-V_G characteristics of a C_{60} single crystal EDLT out to $V_G = 4$ V. (d) Corresponding $I_{disp}-V_G$ measurement. Solid and open blue circles represent electron density n upon charging and discharging, respectively. The voltage sweep rate is 20 mV s^{-1}.

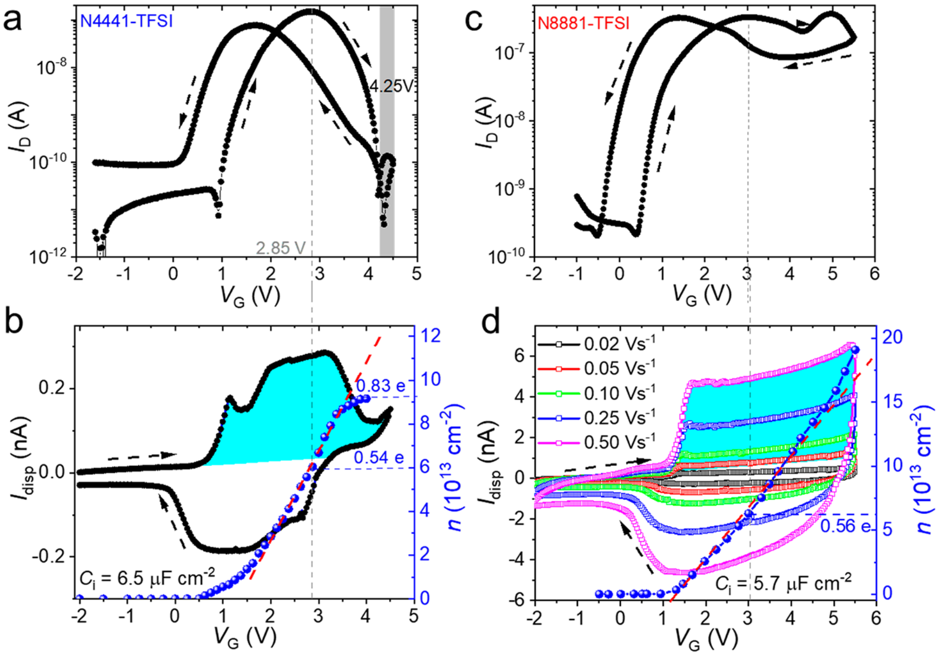

Figure 3. C_{60} single crystal EDLTs gated with ionic liquids featuring larger cations at 215 K. (a) Semilog I_D-V_G characteristic of an EDLT gated with N4441-TFSI. Maximum $V_G = 4.5$ V and $V_D = 0.2$ V. (b) Corresponding $I_{disp}-V_G$ and $n-V_G$ behavior for gating with N4441-TFSI. (c) Semilog I_D-V_G characteristic of an EDLT gated with N8881-TFSI. Maximum $V_G = 5.5$ V and $V_D = 0.2$ V. (d) Corresponding $I_{disp}-V_G$ and $n-V_G$ behavior for gating with N8881-TFSI. The V_G sweep rate in all panels is 20 mVs^{-1}.

6.5 μF cm^{-2} (see Table 1), somewhat lower than for DEME-TFSI as might be expected based on differences in the cation sizes (capacitance is inversely related to double layer thickness).[50] Overall, the results for the N4441-TFSI gated devices are very similar to those for DEME-TFSI devices (see also Figure S11).

Distinctly different behavior is observed when gating the C_{60} crystal with N8881-TFSI. Figure 3c shows two weak peaks at $V_G = +3$ and $+5$ V in the forward scan of the log I_D-V_G characteristic. The $I_{disp}-V_G$ trace in Figure 3d is also starkly different; it shows absolutely no peak and instead "box-like" traces are evident as a function of sweep rate that are very reminiscent of $I_{disp}-V_G$ traces for vacuum gap single crystal FETs (i.e., devices with very ideal charge accumulation and depletion behavior).[38,51,52] The integration of $I_{disp}-V_G$ does not reveal a plateau, rather n continues to increase approximately linearly with V_G up to $V_G = +5.5$ V, corresponding to a very large total electron accumulation $n = 1.9 \times 10^{14}$ cm^{-2} = 1.7 e/C_{60}, and

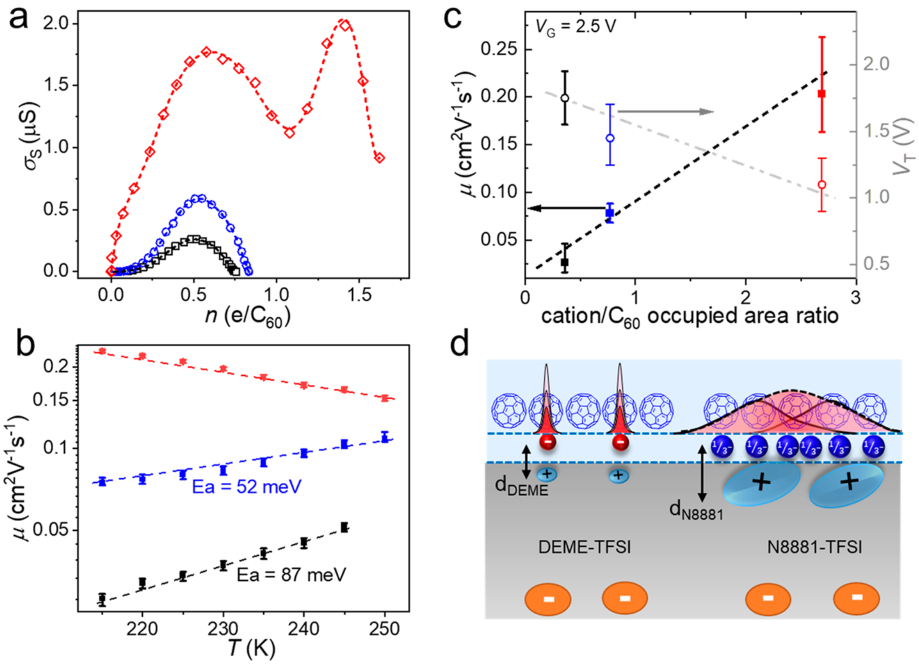

Figure 4. Summary of C_{60} single crystal EDLT behavior as a function of ionic liquid type. (a) Comparison of σ_s−n behavior for C_{60} EDLTs gated with all three ionic liquids (red N8881-TFSI; blue N4441-TFSI; black DEME-TFSI). (b) Dependence of μ and V_T at V_G = 2.5 V on cation size. The error bars represent one standard deviation for at least eight devices tested for each ionic liquid. (c) Temperature-dependent 4-terminal mobility for C_{60} single crystal EDLTs. All devices were cooled to 215 K and then warmed for successive measurements at higher temperatures up to 250 K. (d) Schematic illustration of the electrostatic potential at ionic liquid/C_{60} interfaces with different-sized cations. Smaller cations result in strongly localized electrons in C_{60} crystals. Large cations result in shallower Coulomb potential wells and weaker electron localization.

a double layer capacitance of 5.8 μF cm^{-2} (Table 1 and Figure S12). The double layer capacitance is lower than for the DEME-TFSI and N4441-TFSI devices, consistent with the increased size of the N8881 cation, but we found that we were able to sweep to higher V_G values with the N8881-TFSI ionic liquid, which allowed ∼100% higher charge accumulations (Table 1). Integration of I_{disp} to V_G = +3 V again reveals that the first weak peak in I_D occurs at 0.5 e/C_{60}, as in the other two types of EDLTs. However, there is no dramatic collapse in conductance and no evidence at all of sub-band filling as V_G increases. Partial suppression of I_D at 1 e/C_{60} is followed by a second peak at 1.6 × 10^{14} cm^{-2} = 1.5 e/C_{60} (V_G = 5 V).

A clear comparison of σ_s on a linear scale for the three types of C_{60} EDLTs with different ionic liquids is shown in Figure 4a. Note that all three EDLTs exhibit a conductance maximum near 0.5 e/C_{60} and all three have a minimum near 1 e/C_{60}. In the case of the EDLTs with smaller cations (DEME and N4441), σ_s is completely suppressed near n = 1 e/C_{60}. In contrast, for N8881 devices, σ_s has a soft gap, i.e., incomplete suppression of σ_s at n = 1 e/C_{60} with another peak in σ_s at higher charge density near 1.5 e/C_{60}, as noted above.

Figure 4b shows an additional important result. We have estimated the electron mobility μ for each type of EDLT, using $\mu = \sigma_s/ne$ at V_G = +2.5 V and have measured its temperature dependence over a limited temperature range 215−250 K (Figures S13−S14). One sees in Figure 4b that mobility is clearly activated for the DEME and N4441 devices, but it is band-like for the N8881 EDLTs. The starkly different temperature dependence is consistent with strong carrier localization in the DEME and N4441 gated devices and delocalization in the case of N8881. The four-terminal mobility values are lower in all the EDLTs than in vacuum gap FETs, an effect we have observed previously for rubrene EDLTs, and which is attributable to strong localization effects discussed below,[38,40,43] as well as the known dependence of mobility on gate insulator dielectric constant.[53]

We propose that the unusual conductance versus charge behaviors originate from interactions between ions and carriers in C_{60}, as well as the intrinsic properties of C_{60} itself. The LUMO (conduction) band of face-centered cubic C_{60} is rather narrow, on the order of 0.5 eV,[54−58] and thus one anticipates that Coulomb interactions between electrons and cations, as well as electron−electron interactions, will be important, particularly at the extremely high interfacial charge densities achieved here.[40,42] Indeed, our data indicate a correlation of transport with the cation radius—a larger radius leads to higher overall σ_s (see Table 1 and Figure S15), higher mobility, smaller threshold voltage V_T (Figure 4c), and weaker conductance suppression at n = 1 e/C_{60}—which is consistent with the important role of Coulomb interactions.[40,50]

The maximum in conductance at n = 0.5e/C_{60} and full suppression near n = 1 e/C_{60} for the DEME and N4441 cases can be explained by supposing that electrons are strongly localized on the surfaces of the C_{60} crystals (Figure 4d). A natural cause for the localization would be the electron-cation Coulomb attraction, which is especially strong for the EDLT systems with DEME or N4441 cations in which the cation radii $r_{cation} < r_{C60}$. We estimate this attraction could be as high as 0.5 eV, certainly comparable to the LUMO bandwidth. We anticipate that this interaction breaks the usual triple degeneracy of the neutral C_{60} LUMO.[54,57,58] In this picture, we suppose that each electron is localized on a single C_{60} molecule and conductance is maximized when half the C_{60} molecules are charged (Figure 4d). This would correspond to 1/4 filling of the nondegenerate LUMO band.[59] Likewise, conductance will be minimized when all C_{60} molecules have charge—the 1/2

LUMO band filling condition—because the Coulomb penalty to put two electrons on a C_{60} exceeds the LUMO bandwidth. According to the Mott-Hubbard model, which is the most common model used to study the effect of on-site electron−electron repulsion in solids, an integer number of conduction electrons per site (in this case a C_{60} molecule) leads to a more "strongly correlated" phase.[60] This phase can be either a correlated metal, where the electron mobility is lower than for noninteger filling, or a Mott insulator. In this picture we envision that the on-site Coulomb repulsion (Hubbard U) opens up a Mott-Hubbard-like gap and splits the nondegenerate LUMO band into upper and lower sub-bands.[60] We emphasize that the $I_{\text{disp}}-V_G$ data support the presence of a lower sub-band. The $I_{\text{disp}}-V_G$ traces in Figures 2d and 3b are signatures of the interfacial 2D DOS and thus the suppression of I_{disp}—not just σ_s—at ~1 e/C_{60} is commensurate with reaching the 1/2 band filling condition, i.e., complete filling of the lower sub-band. Importantly, the conventional Mott-Hubbard model involves only electron−electron interactions and not electron−ion interactions, which are clearly at play. Thus, it is likely that the simple Mott framework cannot provide a full description of electronic structure and transport in C_{60} EDLTs; a complete description must also include the effects of the proximal ions and will require further theoretical and experimental investigation. We expect that the cations produce a corrugated potential at the crystal/ionic liquid interface that may be disordered, or ordered, depending on the accumulated interfacial charge.[44] This potential energy landscape will be pronounced for the smaller DEME and N4441 cations, and it seems reasonable that this potential, combined with the Hubbard electron−electron interaction, causes the strongly insulating state near 1 e/C_{60}.[61,62]

When the cation radius increases in the case of N8881-based EDLTs, the physical situation changes markedly. The mobility data indicate accumulated electrons are delocalized, and we suggest that this implies that the corrugation potential from the cations is now greatly diminished. Such a situation may provide better opportunity for observing the effects of electron−electron interactions. Indeed, in contrast to the DEME and N4441 EDLTs, full suppression of conductance at n = 1 e/C_{60} no longer occurs, at least near 215 K where our measurements were made. Instead, Figure 4a shows that a soft gap is present, which may signal that the Hubbard gap is comparable to the thermal energy. Additional low temperature measurements are necessary to confirm whether full suppression of σ_s occurs at n = 1 e/C_{60} where $U > k_BT$; those efforts are ongoing. However, the weak suppression of conductance near 1 e/C_{60} is strong evidence that correlated electron physics is involved. Within the Mott-Hubbard model, another maximum in conductance may be expected at $n \sim 1.5$ e/C_{60}, precisely as we observe for EDLTs gated with N8881-TFSI, corresponding to half-filling of the upper sub-band and 3/4 filling of the full LUMO band.

CONCLUSIONS

In summary, we have employed EDLTs to examine 2D transport in C_{60} single crystals at very large surface charge densities up to and beyond 10^{14} cm^{-2} or 1 electron/C_{60}. We observe clear evidence of strong ion−electron and electron−electron interactions in these systems, and in particular we observe a pronounced peak in the σ_s-n relationship for C_{60} single crystals gated with two ionic liquids, DEME-TFSI and N4441-TFSI. The peak occurs at surface electron accumulations near n = 0.5e/C_{60} with full suppression of σ_s near n = 1 e/C_{60}. Changing the ionic liquid to N8881-TFSI, which features a substantially larger cation, results in two significant changes. First, we find that it substantially improves σ_s and results in much weaker suppression of σ_s at n = 1 e/C_{60}. Second, we are able to sweep V_G out to much larger values, enabling electron accumulations in excess of 10^{14} cm^{-2}. Under these conditions, two conductance peaks become visible, one centered at n = 0.5 e/C_{60} and the other near n = 1.5 e/C_{60}. The clear dependence of the transport on choice of cation demonstrates the importance of carrier−ion interactions in C_{60} EDLTs, an observation that parallels the known effects of counterion type on conduction in organic charge-transfer salts.[59] We believe the σ_s-n behavior in C_{60} EDLTs is impacted by both Mott physics and the corrugation potential associated with the cations in the electrical double layer. The corrugation potential is a key difference from the conventional Mott picture. Importantly, increasing the cation radius of the ionic liquid diminishes the corrugation, leading to higher conductance and revealing a soft energy gap at 215 K. Future experiments will focus on obtaining complete σ_s-T measurements as a function of n so that the transport and electronic phase behavior can be assessed thoroughly. A primary message of the current study is that choice of ionic liquid is critical and that ion-carrier effects abound. Additionally, our results reinforce earlier findings that conductance peaks are a general feature of electrolyte-gated organic semiconductors,[37−42] likely because their narrow bands and low dielectric constants make them especially susceptible to Coulombic effects. We believe that organic single crystal EDLTs have promising potential as platforms for exploring the onset of metallicity in organic semiconductors as a function of continuously tunable charge and counterion type. Such work will complement the extensive literature on charge transfer salts where transport and electronic phase behavior are known to be strongly correlated with choice of counterions.[63]

METHODS AND EXPERIMENTAL SECTION

Device Fabrication and Electrical Measurement. C_{60} was purchased from Sigma-Aldrich. Single crystals were grown by the physical vapor transport (PVT) method and then laminated onto prepatterned Au-coated PDMS substrates featuring source, drain, gate and channel electrodes to make four-terminal air-gap FETs. All contact electrodes consisted of Cr (3 nm)/Au (20 nm) bilayer films. The distance between the source and drain electrodes was 300 μm, and the distance between the two-channel measurement electrodes (V_1 and V_2) was 150 μm. The gate-to-crystal gap was 5 μm for all devices. EDLTs were constructed based on the air-gap FETs by filling the gap between the C_{60} single crystal and the gate with ionic liquid by capillary action. The ionic liquids were obtained from Merck KGaA. The $I-V$ characteristics of the devices were measured in an N_2-filled glovebox, and variable temperature measurements were carried out in the dark with a cryogenic probe station at 10^{-4} Torr. The displacement currents were recorded with a Keithley 2612 source measure unit, which swept the voltage between the gate and the shorted source and drain contacts while measuring the current.

Characterization. High-resolution X-ray diffraction (XRD) was carried out with a Philips Panalytical X'Pert Pro diffractometer with monochromatic Cu Kα radiation (wavelength 0.154 nm) at tube settings of 45 kV and 40 mA. Topography and surface potential images were collected with a Bruker Instruments Nanoscope V Multimode AFM with conductive probes from Mikromasch USA (NSC18, Pt coated, resonant frequency 60−90 kHz, k = 2−5.5 N/m).

ASSOCIATED CONTENT

Supporting Information

The Supporting Information is available free of charge at https://pubs.acs.org/doi/10.1021/acsnano.2c00222.

Description of crystal growth, scanning Kelvin probe microscopy (SKPM) images, device fabrication, temperature dependence of the capacitance−frequency (C−F) behavior, transfer curves of a C_{60} single crystal vacuum gap device and EDLTs at room temperature, contact resistance measurements, transfer characteristics (I_D−V_G) and electron density versus gate voltage (n−V_G), temperature dependence of the sheet conductance (σ_s−T) using different ionic liquids, and the corresponding the relationship between σ_s and the size of cations (PDF)

AUTHOR INFORMATION

Corresponding Authors

Tao He − *State Key Laboratory of Crystal Materials, Shandong University, 250100 Jinan, Shandong, People's Republic of China; Department of Chemical Engineering and Materials Science, University of Minnesota, Minneapolis, Minnesota 55455, United States;* orcid.org/0000-0002-3308-9107; Email: the@sdu.edu.cn

C. Daniel Frisbie − *Department of Chemical Engineering and Materials Science, University of Minnesota, Minneapolis, Minnesota 55455, United States;* orcid.org/0000-0002-4735-2228; Email: frisbie@umn.edu

Complete contact information is available at: https://pubs.acs.org/10.1021/acsnano.2c00222

Author Contributions

C.D.F. designed and guided the research program. T.H. grew single crystals, fabricated the devices, and performed measurements and analysis. T.H. and C.D.F. wrote the manuscript.

Notes

The authors declare no competing financial interest.

ACKNOWLEDGMENTS

This work was primarily supported by the MRSEC program of the National Science Foundation under Grant Number DMR-2011401. T.H. also acknowledges the National Natural Science Foundation of China Grant 62074093. C.D.F. acknowledges partial support from NSF through the National Nano Coordinated Infrastructure (NNCI) Network, under Award Number ECCS-2025124. T.H. also acknowledges support from the Qilu Young Scholars Program of Shandong University and Shandong Taishan Young Expert Program (tsqn201909027). C.D.F. thanks Merck for supplying the ionic liquids and Chris Leighton and Turan Birol of the University of Minnesota for stimulating discussions and comments on the manuscript.

REFERENCES

(1) Saito, Y.; Nojima, T.; Iwasa, Y. Highly Crystalline 2D Superconductors. *Nat. Rev. Mater.* **2017**, *2*, 16094.

(2) Bisri, S. Z.; Shimizu, S.; Nakano, M.; Iwasa, Y. Endeavor of Iontronics: From Fundamentals to Applications of Ion-Controlled Electronics. *Adv. Mater.* **2017**, *29*, 1607054.

(3) Du, H.; Lin, X.; Xu, Z.; Chu, D. Electric Double-Layer Transistors: a Review of Recent Progress. *J. Mater. Sci.* **2015**, *50*, 5641−5673.

(4) Leighton, C. Electrolyte-Based Ionic Control of Functional Oxides. *Nat. Mater.* **2019**, *18*, 13−18.

(5) Yamada, Y.; Ueno, K.; Fukumura, T.; Yuan, H. T.; Shimotani, H.; Iwasa, Y.; Gu, L.; Tsukimoto, S.; Ikuhara, Y.; Kawasaki, M. Electrically Induced Ferromagnetism at Room Temperature in Cobalt-Doped Titanium Dioxide. *Science* **2011**, *332*, 1065−1067.

(6) Walter, J.; Charlton, T.; Ambaye, H.; Fitzsimmons, M. R.; Orth, P. P.; Fernandes, R. M.; Leighton, C. Giant Rlectrostatic Modification of Magnetism via Electrolyte-Gate-Induced Cluster Percolation in $La_{1-x}Sr_xCoO_{3-\delta}$. *Phys. Rev. Mater.* **2018**, *2*, 111406.

(7) Jeong, J.; Aetukuri, N.; Graf, T.; Schladt, T. D.; Samant, M. G.; Parkin, S. S. P. Suppression of Metal-Insulator Transition in VO_2 by Electric Field−Induced Oxygen Vacancy Formation. *Science* **2013**, *339*, 1402−1405.

(8) Ueno, K.; Nakamura, S.; Shimotani, H.; Yuan, H. T.; Kimura, N.; Nojima, T.; Aoki, H.; Iwasa, Y.; Kawasaki, M. Discovery of Superconductivity in $KTaO_3$ by Electrostatic Carrier Doping. *Nat. Nanotechnology* **2011**, *6*, 408−412.

(9) Ueno, K.; Nakamura, S.; Shimotani, H.; Ohtomo, A.; Kimura, N.; Nojima, T.; Aoki, H.; Iwasa, Y.; Kawasaki, M. Electric-Field-Induced Superconductivity in an Insulator. *Nat. Mater.* **2008**, *7*, 855−858.

(10) Yuan, H. T.; Shimotani, H.; Tsukazaki, A.; Ohtomo, A.; Kawasaki, M.; Iwasa, Y. High-Density Carrier Accumulation in ZnO Field-Effect Transistors Gated by Electric Double Layers of Ionic Liquids. *Adv. Funct. Mater.* **2009**, *19*, 1046−1053.

(11) Scherwitzl, R.; Zubko, P.; Lezama, I. G.; Ono, S.; Morpurgo, A. F.; Catalan, G.; Triscone, J.-M. Electric-Field Control of the Metal-Insulator Transition in Ultrathin $NdNiO_3$ Films. *Adv. Mater.* **2010**, *22*, 5517−5520.

(12) Li, L. J.; O'Farrell, E. C.; Loh, K. P.; Eda, G.; Ozyilmaz, B.; Castro Neto, A. H. Controlling Many-Body States by the Electric-Field Effect in a Two-Dimensional Material. *Nature* **2016**, *529*, 185−189.

(13) Katase, T.; Hiramatsu, H.; Kamiya, T.; Hosono, H. Electric Double-Layer Transistor Using Layered Iron Selenide Mott Insulator $TlFe_{1.6}Se_2$. *Proc. Natl. Acad. Sci. U. S. A.* **2014**, *111*, 3979−3983.

(14) Shi, W.; Ye, J.; Zhang, Y.; Suzuki, R.; Yoshida, M.; Miyazaki, J.; Inoue, N.; Saito, Y.; Iwasa, Y. Superconductivity Series in Transition Metal Dichalcogenides by Ionic Gating. *Sci. Rep.* **2015**, *5*, 12534.

(15) Ovchinnikov, D.; Gargiulo, F.; Allain, A.; Pasquier, D. J.; Dumcenco, D.; Ho, C. H.; Yazyev, O. V.; Kis, A. Disorder Engineering and Conductivity Dome in ReS_2 with Electrolyte Gating. *Nat. Commun.* **2016**, *7*, 12391.

(16) Shiogai, J.; Ito, Y.; Mitsuhashi, T.; Nojima, T.; Tsukazaki, A. Electric-Field-Induced Superconductivity in Electrochemically Etched Ultrathin FeSe Films on $SrTiO_3$ and MgO. *Nat. Phys.* **2016**, *12*, 42−46.

(17) Lu, J.; Zheliuk, O.; Chen, Q.; Leermakers, I.; Hussey, N. E.; Zeitler, U.; Ye, J. Full Superconducting Dome of Strong Ising Protection in Gated Monolayer WS_2. *Proc. Natl. Acad. Sci. U. S. A.* **2018**, *115*, 3551−3556.

(18) Walter, J.; Voigt, B.; Day-Roberts, E.; Heltemes, K.; Fernandes, R. M.; Birol, T.; Leighton, C. Voltage-Induced Ferromagnetism in a Diamagnet. *Sci. Adv.* **2020**, *6*, 7721.

(19) Gonnelli, R. S.; Piatti, E.; Sola, A.; Tortello, M.; Dolcini, F.; Galasso, S.; Nair, J. R.; Gerbaldi, C.; Cappelluti, E.; Bruna, M.; Ferrari, A. C. Weak Localization in Electric-Double-Layer Gated Few-Layer Graphene. *2D Mater.* **2017**, *4*, 035006.

(20) Ye, J. T.; Craciun, M. F.; Koshino, M.; Russo, S.; Inoue, S.; Yuan, H. T.; Shimotani, H.; Morpurgo, A. F.; Iwasa, Y. Accessing the Transport Properties of Graphene and Its Multilayers at High Carrier Density. *Proc. Natl. Acad. Sci. U. S. A.* **2011**, *108*, 13002−13006.

(21) Ren, X.; Wang, Y.; Xie, Z.; Xue, F.; Leighton, C.; Frisbie, C. D. Gate-Tuned Insulator−Metal Transition in Electrolyte-Gated Transistors Based on Tellurene. *Nano Lett.* **2019**, *19*, 4738−4744.

(22) Wang, Y.; Qiu, G.; Wang, R.; Huang, S.; Wang, Q.; Liu, Y.; Du, Y.; Goddard, W. A.; Kim, M. J.; Xu, X.; Ye, P. D.; Wu, W. Field-Effect Transistors Made From Solution-Grown Two-Dimensional Tellurene. *Nat. Electron.* **2018**, *1*, 228−236.

(23) Ye, J. T.; Zhang, Y. J.; Akashi, R.; Bahramy, M. S.; Arita, R.; Iwasa, Y. Superconducting Dome in a Gate-Tuned Band Insulator. *Science* **2012**, *338*, 1193−1196.

(24) Kawasugi, Y.; Seki, K.; Edagawa, Y.; Sato, Y.; Pu, J.; Takenobu, T.; Yunoki, S.; Yamamoto, H. M.; Kato, R. Simultaneous Enhancement of Conductivity and Seebeck Coefficient in an Organic Mott Transistor. *Appl. Phys. Lett.* **2016**, *109*, 233301.

(25) Kawasugi, Y.; Seki, K.; Edagawa, Y.; Sato, Y.; Pu, J.; Takenobu, T.; Yunoki, S.; Yamamoto, H. M.; Kato, R. Electron−Hole Doping

Asymmetry of Fermi Surface Reconstructed in a Simple Mott Insulator. *Nat. Commun.* **2016**, *7*, 12356.

(26) Kawasugi, Y.; Seki, K.; Tajima, S.; Pu, J.; Takenobu, T.; Yunoki, S.; Yamamoto, H. M.; Kato, R. Two-Dimensional Ground-State Mapping of a Mott-Hubbard System in a Flexible Field-Effect Device. *Sci. Adv.* **2019**, *5*, eaav7282.

(27) Kawasugi, Y.; Masuda, H.; Pu, J.; Takenobu, T.; Yamamoto, H. M.; Kato, R.; Tajima, N. Electric Double Layer Doping of Charge-Ordered Insulators α-(BEDT-TTF)$_2$I$_3$ and α-(BETS)$_2$I$_3$. *Crystals* **2021**, *11*, 791.

(28) Kasuya, N.; Tsurumi, J.; Okamoto, T.; Watanabe, S.; Takeya, J. Two-Dimensional Hole Gas in Organic Semiconductors. *Nat. Mater.* **2021**, *20*, 1401−1406.

(29) Mitrano, M.; Cantaluppi, A.; Nicoletti, D.; Kaiser, S.; Perucchi, A.; Lupi, S.; Di Pietro, P.; Pontiroli, D.; Riccò, M.; Clark, S. R.; Jaksch, D.; Cavalleri, A. Possible Light-Induced Superconductivity in K_3C_{60} at High Temperature. *Nature* **2016**, *530*, 461−464.

(30) Hebard, A. F.; Rosseinsky, M. J.; Haddon, R. C.; Murphy, D. W.; Glarum, S. H.; Palstra, T. T. M.; Ramirez, A. P.; Kortan, A. R. Superconductivity at 18 K in Potassium-Doped C_{60}. *Nature* **1991**, *350*, 600−601.

(31) Tanigaki, K.; Ebbesen, T. W.; Saito, S.; Mizuki, J.; Tsai, J. S.; Kubo, Y.; Kuroshima, S. Superconductivity at 33 K in $Cs_xRb_yC_{60}$. *Nature* **1991**, *352*, 222−223.

(32) Fleming, R. M.; Ramirez, A. P.; Rosseinsky, M. J.; Murphy, D. W.; Haddon, R. C.; Zahurak, S. M.; Makhija, A. V. Relation of Structure and Superconducting Transition Temperatures in A_3C_{60}. *Nature* **1991**, *352*, 787−788.

(33) Stepniak, F.; Benning, P. J.; Poirier, D. M.; Weaver, J. H. Electrical Transport in Na, K, Rb, and Cs Fullerides: Phase Formation, Microstructure, and Metallicity. *Phys. Rev. B* **1993**, *48*, 1899−1906.

(34) Haddon, R. C. Electronic Structure, Conductivity and Superconductivity of Alkali Metal Doped C_{60}. *Pure Appl. Chem.* **1993**, *65*, 11−15.

(35) Zhou, O.; Fischer, J. E.; Coustel, N.; Kycia, S.; Zhu, Q.; McGhie, A. R.; Romanow, W. J.; McCauley, J. P.; Smith, A. B.; Cox, D. E. Structure and Bonding in Alkali-Metal-Doped C_{60}. *Nature* **1991**, *351*, 462−464.

(36) Zadik, R. H.; Takabayashi, Y.; Klupp, G.; Colman, R. H.; Ganin, A. Y.; Potočnik, A.; Jeglič, P.; Arčon, D.; Matus, P.; Kamarás, K.; Kasahara, Y.; Iwasa, Y.; Fitch, A. N.; Ohishi, Y.; Garbarino, G.; Kato, K.; Rosseinsky, M. J.; Prassides, K. Optimized Unconventional Superconductivity in a Molecular Jahn-Teller Metal. *Sci. Adv.* **2015**, *1*, e1500059.

(37) Ofer, D.; Crooks, R. M.; Wrighton, M. S. Potential Dependence of the Conductivity of Highly Oxidized Polythiophenes, Polypyrroles, and Polyaniline: Finite Windows of High Conductivity. *J. Am. Chem. Soc.* **1990**, *112*, 7869−7879.

(38) Xie, W.; Frisbie, C. D. Organic Electrical Double Layer Transistors Based on Rubrene Single Crystals: Examining Transport at High Surface Charge Densities Above 10^{13} cm^{-2}. *J. Phys. Chem. C* **2011**, *115*, 14360−14368.

(39) Paulsen, B. D.; Frisbie, C. D. Dependence of Conductivity on Charge Density and Electrochemical Potential in Polymer Semiconductors Gated with Ionic Liquids. *J. Phys. Chem. C* **2012**, *116*, 3132−3141.

(40) Xia, Y.; Xie, W.; Ruden, P. P.; Frisbie, C. D. Carrier Localization on Surfaces of Organic Semiconductors Gated with Electrolytes. *Phys. Rev. Lett.* **2010**, *105*, 036802.

(41) Xie, W.; Wang, S.; Zhang, X.; Leighton, C.; Frisbie, C. D. High Conductance 2D Transport around the Hall Mobility Peak in Electrolyte-Gated Rubrene Crystals. *Phys. Rev. Lett.* **2014**, *113*, 246602.

(42) Xie, W.; Liu, F.; Shi, S.; Ruden, P. P.; Frisbie, C. D. Charge Density Dependent Two-Channel Conduction in Organic Electric Double Layer Transistors (EDLTs). *Adv. Mater.* **2014**, *26*, 2527−2532.

(43) Ono, S.; Miwa, K.; Seki, S.; Takeya, J. A Comparative Study of Organic Single-Crystal Transistors Gated with Various Ionic-Liquid Electrolytes. *Appl. Phys. Lett.* **2009**, *94*, 063301.

(44) Black, J. M.; Come, J.; Bi, S.; Zhu, M.; Zhao, W.; Wong, A. T.; Noh, J. H.; Pudasaini, P. R.; Zhang, P.; Okatan, M. B.; Dai, S.; Kalinin, S. V.; Rack, P. D.; Ward, T. Z.; Feng, G.; Balke, N. Role of Electrical Double Layer Structure in Ionic Liquid Gated Devices. *ACS Appl. Mater. Interfaces* **2017**, *9*, 40949−40958.

(45) Nelson, J.; Reich, K. V.; Sammon, M.; Shklovskii, B. I.; Goldman, A. M. Hopping Conduction via Ionic Liquid Induced Silicon Surface States. *Phys. Rev. B* **2015**, *92*, 085424.

(46) He, T.; Wu, Y.; D'Avino, G.; Schmidt, E.; Stolte, M.; Cornil, J.; Beljonne, D.; Ruden, P. P.; Wurthner, F.; Frisbie, C. D. Crystal Step Edges Can Trap Electrons on the Surfaces of N-Type Organic Semiconductors. *Nat. Commun.* **2018**, *9*, 2141.

(47) Lauw, Y.; Horne, M. D.; Rodopoulos, T.; Nelson, A.; Leermakers, F. A. M. Electrical Double-Layer Capacitance in Room Temperature Ionic Liquids: Ion-Size and Specific Adsorption Effects. *J. Phys. Chem. B* **2010**, *114*, 11149−11154.

(48) Benning, P. J.; Martins, J. L.; Weaver, J. H.; Chibante, L. P. F.; Smalley, R. E. Electronic States of K_xC_{60}: Insulating, Metallic, and Superconducting Character. *Science* **1991**, *252*, 1417−1419.

(49) Gu, C.; Stepniak, F.; Poirier, D. M.; Jost, M. B.; Benning, P. J.; Chen, Y.; Ohno, T. R.; Martins, J. L.; Weaver, J. H.; Fure, J.; Smalley, R. E. Metallic and Insulating Phases of Li_xC_{60}, Na_xC_{60}, and Rb_xC_{60}. *Phys. Rev. B* **1992**, *45*, 6348−6351.

(50) Ono, S.; Miwa, K.; Seki, S. Determination of Optimal Ionic Liquid for Organic Single-Crystal Field-Effect Transistors. *Appl. Phys. Lett.* **2016**, *108*, 063301.

(51) Noguchi, Y.; Miyazaki, Y.; Tanaka, Y.; Sato, N.; Nakayama, Y.; Schmidt, T. D.; Brütting, W.; Ishii, H. Charge Accumulation at Organic Semiconductor Interfaces Due to a Permanent Dipole Moment and Its Orientational Order in Bilayer Devices. *J. Appl. Phys.* **2012**, *111*, 114508.

(52) Liang, Y.; Frisbie, C. D.; Chang, H.-C.; Ruden, P. P. Conducting Channel Formation and Annihilation in Organic Field-Effect Structures. *J. Appl. Phys.* **2009**, *105*, 024514.

(53) Hulea, I. N.; Fratini, S.; Xie, H.; Mulder, C. L.; Iossad, N. N.; Rastelli, G.; Ciuchi, S.; Morpurgo, A. F. Tunable Frohlich Polarons in Organic Single-Crystal Transistors. *Nat. Mater.* **2006**, *5*, 982−986.

(54) Saito, S.; Oshiyama, A. Cohesive Mechanism and Energy Bands of Solid C_{60}. *Phys. Rev. Lett.* **1991**, *66*, 2637−2640.

(55) Merkel, M.; Knupfer, M.; Golden, M. S.; Fink, J.; Seemann, R.; Johnson, R. L. Photoemission Study of the Electronic Structure of C_{60} and K_xC_{60}. *Phys. Rev. B* **1993**, *47*, 11470−11478.

(56) Tjeng, L. H.; Hesper, R.; Heessels, A. C. L.; Heeres, A.; Jonkman, H. T.; Sawatzky, G. A. Development of the Electronic Structure in a K-Doped C_{60} Monolayer on a Ag (1 1 1) Surface. *Solid State Commun.* **1997**, *103*, 31−35.

(57) Gunnarsson, O. Superconductivity in Fullerides. *Rev. Mod. Phys.* **1997**, *69* (2), 575−606.

(58) Iwasa, Y.; Takenobu, T. Superconductivity, Mott Hubbard States, and Molecular Orbital Order in Intercalated Fullerides. *J. Phys.: Condens. Matter* **2003**, *15*, R495−R519.

(59) Mori, T. Organic Conductors with Unusual Band Fillings. *Chem. Rev.* **2004**, *104*, 4947−4970.

(60) Mott, N. *Metal-insulator transitions*, 1st ed.; CRC Press, London, 1990.

(61) Tie, M.; Dhirani, A. A. Electrolyte-Gated Charge Transport in Molecularly Linked Gold Nanoparticle Films: The Transition From a Mott Insulator to an Exotic Metal with Strong Electron-Electron Interactions. *J. Chem. Phys.* **2016**, *145*, 104702.

(62) Unruh, D.; Camjayi, A.; Hansen, C.; Bobadilla, J.; Rozenberg, M. J.; Zimanyi, G. T. Disordered Mott−Hubbard Physics in Nanoparticle Solids: Transitions Driven by Disorder, Interactions, and Their Interplay. *Nano Lett.* **2020**, *20*, 8569−8575.

(63) Pouget, J.-P.; Alemany, P.; Canadell, E. Donor-Anion Interactions in Quarter-Filled Low-Dimensional Organic Conductors. *Mater. Horiz.* **2018**, *5*, 590−640.